

# Topology and pressure distribution reconstruction of an englacial channel

Laura Piho<sup>1</sup>, Andreas Alexander<sup>2</sup>, and Maarja Kruusmaa<sup>3</sup>

<sup>1</sup>Tallinn University of Technology

<sup>2</sup>University of Oslo

<sup>3</sup>Tallinna Tehnikaülikool, Tallinna Tehnikaülikool

November 24, 2022

## Abstract

Glacial hydrology describes the way water moves over, through and under glaciers. Meltwater flows every summer over the surface of glaciers and ice sheets, creating pathways down to below the surface, eventually reaching the glacier bed and thereby influencing ice motion. Glacier and ice sheet models, trying to predict their future sea-level rise contribution, need to therefore be able to properly describe glacial hydrological processes. However, the current knowledge in the field is still limited due to the lack of measurement technology for subsurface in situ flow observations. Here we present a measurement method that allows to reconstruct planar subsurface water flow paths and spatially reference water pressures therein. The approach uses inertial measurements from submersible sensing drifters and reconstructs the flow path from given start and end coordinates. Validation cases show an average error of 3.90 m compared to GNSS reference. We showcase this method by reconstructing the flow path and the spatial water pressure distribution of an englacial channel on Austre Brøggerbreen (Svalbard). The average error of the reconstruction is thereby 12.1 m and the average pressure error 3.4 mbar (0.3%). Our method will allow to study en- and subglacial flow paths and the pressure distribution therein, thereby allowing for model validation and activation. Further on, our method also allows to reconstruct other subsurface fluid flow paths, when a global spatial reference (e.g. GNSS) is not available.

1 **Topology and pressure distribution reconstruction of an**  
2 **englacial channel**

3 **Laura Piho<sup>1,\*</sup>, Andreas Alexander<sup>2,3,\*</sup>, Maarja Kruusmaa<sup>1,4</sup>**

4 <sup>1</sup>Centre for Biorobotics, Tallinn University of Technology

5 <sup>2</sup>Department of Geosciences, University of Oslo

6 <sup>3</sup>Department of Arctic Geology, The University Centre in Svalbard

7 <sup>4</sup>Centre for Autonomous Marine Operations and Systems, Norwegian University of Science and

8 Technology

9 \*Shared co-first authorship

10 **Key Points:**

- 11 • We present a method to reconstruct subsurface water flows from *in situ* mea-  
12 surements with sensing drifters
- 13 • We showcase the method with the reconstruction of the flow path and the  
14 spatial water pressure distribution of an englacial channel
- 15 • Our methods opens up new ways to study en- and subglacial drainage systems  
16 and other subsurface fluid flow paths

---

Corresponding author: Andreas Alexander, [andreas.alexander@geo.uio.no](mailto:andreas.alexander@geo.uio.no)

## Abstract

Glacial hydrology describes the way water moves over, through and under glaciers. Meltwater flows every summer over the surface of glaciers and ice sheets, creating pathways down to below the surface, eventually reaching the glacier bed and thereby influencing ice motion. Glacier and ice sheet models, trying to predict their future sea-level rise contribution, need to therefore be able to properly describe glacial hydrological processes. However, the current knowledge in the field is still limited due to the lack of measurement technology for subsurface *in situ* flow observations. Here we present a measurement method that allows to reconstruct planar subsurface water flow paths and spatially reference water pressures therein. The approach uses inertial measurements from submersible sensing drifters and reconstructs the flow path from given start and end coordinates. Validation cases show an average error of 3.90 m compared to GNSS reference. We showcase this method by reconstructing the flow path and the spatial water pressure distribution of an englacial channel on Austre Brøggerbreen (Svalbard). The average error of the reconstruction is thereby 12.1 m and the average pressure error 3.4 mbar (0.3%). Our method will allow to study en- and subglacial flow paths and the pressure distribution therein, thereby allowing for model validation and activation. Further on, our method also allows to reconstruct other subsurface fluid flow paths, when a global spatial reference (e.g. GNSS) is not available.

## Plain Language Summary

The imprecision of glacier and ice sheets models is a major contributor to the uncertainty of future sea level rise predictions. This uncertainty is partly caused by the lack of *in situ* observations from subsurface hydrology where simultaneous records of subsurface water flow paths and the pressures within are highly relevant. We present a method to reconstruct subsurface flow paths from inertia sensing drifter measurements and align readings of pressure sensors to them. Our results open up new ways to measure in previously inaccessible environments and can thus contribute data, not only for model validation and calibration, but also for model activation.

## 1 Introduction

Predictions about future sea-level rise are uncertain, as outlined in the recent IPCC report (Pörtner et al., 2019). The uncertainty rises partly from our incomplete understanding of glacier and ice sheet dynamics, where glacier hydrology plays a key role. Our incomplete knowledge of glacier hydrology is mostly caused by lack of direct observations of the en- and subglacial environment, making it hard to constrain, yet verify theoretical and numerical models (Hooke, 1989; Flowers, 2015a, 2015b). Even though hydrological glacier models have made tremendous progress in the recent years, their calibration still remains difficult (Flowers, 2015a).

Water can generally transit through and under glaciers and ice sheets in en- and subglacial drainage systems. The physical configuration of these drainage systems varies between individual glaciers and ice sheets, as well as on spatial and temporal scale (Hubbard & Nienow, 1997; Fountain & Walder, 1998). Even the most sophisticated hydrological models, simulating the behavior of the hydrological system and linking it to ice dynamics, employ the basic concepts of hydraulic potentials (Shreve, 1972) and the physical principles laid out by Röthlisberger (Röthlisberger, 1972) almost 50 years ago (see Flowers (2015a) for a review of current models). The theory of hydraulic potential is thereby utilizing glacier geometry to calculate hypothetical water pathways (Shreve, 1972; Björnsson, 1975). Fluxes are often expressed empirically as a function of the hydraulic potential, where several parameters need

67 to be determined empirically by the modeler (Flowers, 2015a). The lack of direct  
68 observations makes it thereby hard to validate the choice of model parameters, thus  
69 contributing to the uncertainty of the models.

70 Over the years, a broad spectrum of methods for studying inaccessible subsur-  
71 face flows has been developed in glaciology. Typical empirical research approaches  
72 for temperate alpine glaciers include: investigations of bulk meltwater discharge and  
73 chemistry, tracer studies, proglacial bedrock investigations and borehole measure-  
74 ments (Hubbard & Nienow, 1997). These techniques are, with the exemption of the  
75 last one, indirect methods, thus not allowing direct measurements of the subsur-  
76 face environment. Previous years have seen the use of time-consuming geophysical  
77 investigation methods, utilizing ground penetrating radar (GPR) (e.g., Stuart et  
78 al., 2003; Bælum & Benn, 2011; Hansen et al., 2020; Schaap et al., 2020) and seis-  
79 mic arrays (Gimbert et al., 2016; Nanni et al., 2020) to locate en- and subglacial  
80 channels. In wintertime, moulins and meltwater channels are accessible for direct  
81 speleological investigations and mapping of water flow paths in shallow glaciers  
82 (e.g., Holmlund, 1988; Vatne, 2001; Gulley et al., 2009; Alexander, Obu, et al., 2020;  
83 Hansen et al., 2020). Water pressures have been indirectly induced from geophysical  
84 models utilizing seismic arrays (Nanni et al., 2020) or directly measured via moulins  
85 and boreholes (e.g., Iken, 1972; Iken & Bindschadler, 1986; Engelhardt et al., 1990;  
86 Hubbard et al., 1995; Stone & Clarke, 1996; Vieli et al., 2004; Andrews et al., 2014).  
87 The latter is, however, point-scale by nature (Flowers, 2015a). Therefore the devel-  
88 opment of new remote sensing methods for direct measurements of basal drainage  
89 parameters over spatial scales is a top research priority to reduce uncertainty of  
90 glacier and ice sheet models (Flowers, 2015a, 2015b).

91 In recent years submersible drifters have been proposed to measure water pres-  
92 sures along the flow path of glacial drainage systems (Bagshaw et al., 2012, 2014;  
93 Alexander, Kruusmaa, et al., 2020). Since the subsurface environments are GPS de-  
94 nied, the recorded data of these platforms lack spatial reference. Previously we have  
95 proposed the use of inertial measurement units (IMUs), containing accelerometers,  
96 gyroscopes and magnetometers, alongside pressure recordings and demonstrated  
97 high repeatability of measurements in a supraglacial channel (Alexander, Kruusmaa,  
98 et al., 2020). In theory, double integration of the recorded acceleration data would  
99 result in travelled distance. In practice, error accumulation and noise lead to high  
100 uncertainty. This is a familiar problem in navigation, known as a dead reckoning  
101 error (Montello, 2005). The double integration error in dead-reckoning grows linearly  
102 if the acceleration offset is small but for a significant acceleration offset, the error  
103 can grow quadratically and very quickly lead to high uncertainty. In mobile robotics  
104 this problem is commonly addressed using probabilistic mapping, localization and  
105 navigation algorithms (Thrun et al., 1998). Uncertainty is further reduced by using  
106 salient features, recognizable by robotic sensors, as landmarks (Thrun, 1998).

107 In this study we use machine-learning extracted features from IMU data as  
108 salient features. The idea for feature extraction is derived from (Fourati et al.,  
109 2013), showing that inertial measurement data can be used to map human move-  
110 ment, as human steps have repeated recognizable periods during which the velocity  
111 and acceleration are zero. In our previous study (Alexander, Kruusmaa, et al., 2020)  
112 we observed distinct signal patterns related to morphology of glacial channels but  
113 could not quantify and classify them to extract salient flow features. In this study,  
114 we propose to solve this problem using an infinite hidden Markov model giving the  
115 probability distribution of features from IMU data. We further propose piece-wise  
116 integration of this data to compute the flow path between the extracted features.  
117 As such, the accumulated integration errors do not grow unbounded. As result, we  
118 obtain a probabilistic track of the channel between two known globally referenced  
119 points (e.g. GNSS referenced deployment and recovery points). Measuring pressure

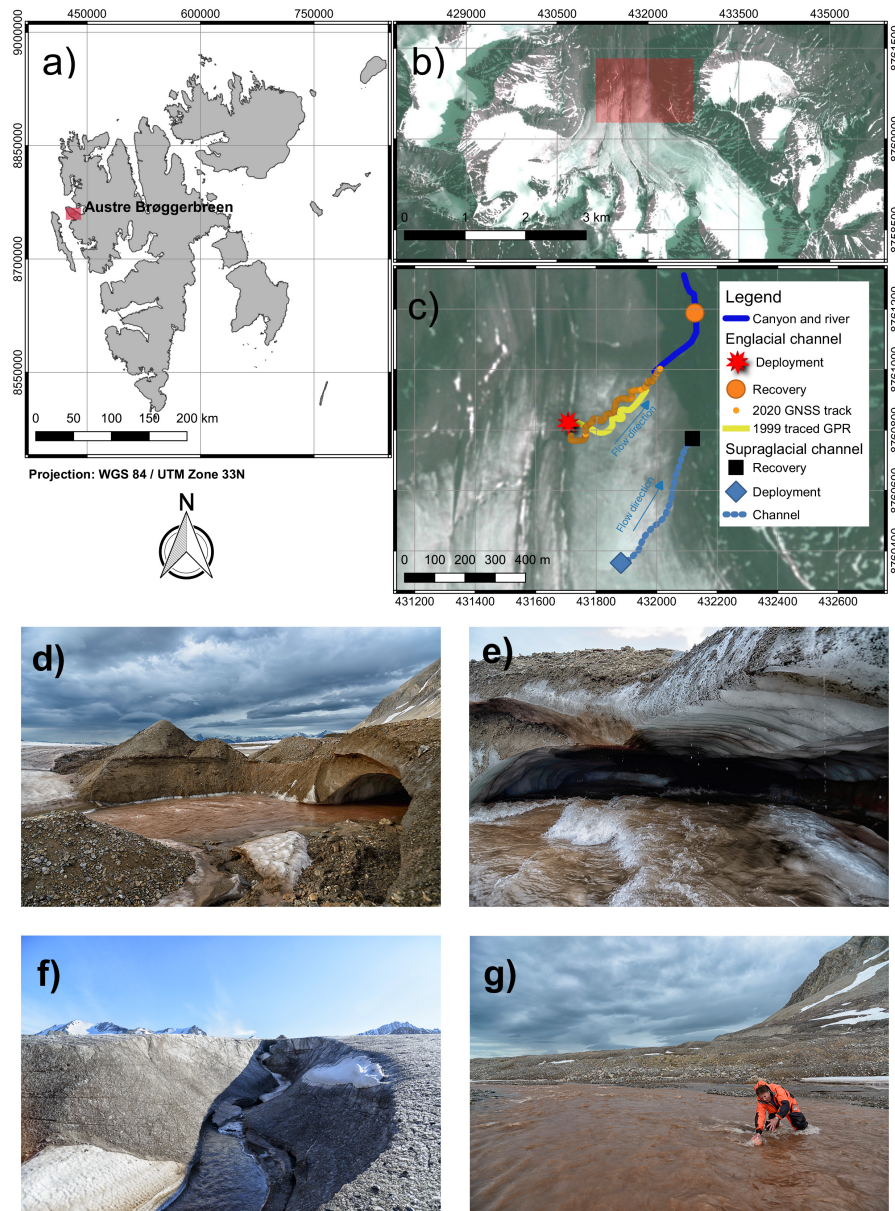


Figure 1: The test site. (a) Location of Austre Brøggerbreen on the Svalbard archipelago. (b) Location of the investigated supra- and englacial channel on the glacier. Background image: Planet Labs, 09.07.2019 (Team Planet, 2017). (c) Map of the studied supra- and englacial channel with flow directions (blue arrows). Shown are the 2019 GNSS track with deployment and recovery point for the supraglacial channel, the 1999 GPR track of the englacial channel from (Stuart et al., 2003), the 2020 GNSS track of the melted out englacial channel, as well as river and canyon section following the englacial channel, mapped out from Planet optical imagery (Team Planet, 2017). Additionally shown are the deployment and recovery points used for drifter deployments at the englacial channel. Background image: Planet Labs, 09.07.2019 (Team Planet, 2017). (d) Deployment point at the englacial channel in 2019. (e) Entrance to the englacial channel in July 2019. (f) Canyon following the outlet of the englacial channel in July 2019. (g) Drifter recovery at the proglacial river in July 2019.

120 along with the IMU data, further allows to spatially reference the pressure distribu-  
121 tion along this track.

122 We showcase the feasibility and applicability of our approach with the recon-  
123 struction of the spatially referenced flow path and the water pressure distribution  
124 of an englacial channel on Austre Brøggerbreen (Svalbard, Norwegian Arctic; see  
125 also fig. 1). Our reconstructions are based on data collected by a submersible drifter  
126 platform containing an IMU as well as pressure sensors and compared to GNSS data  
127 gathered by a GNSS surface drifter. The results are validated by the reconstruction  
128 of a known rectangular path with respect to dGPS and GNSS reference, as well as  
129 with reconstruction of a supraglacial channel (fig. 1(c)) with respect to GNSS ref-  
130 erence. We further qualitatively compare our englacial reconstruction to the results  
131 of an earlier GPR investigation (Stuart et al., 2003), satellite imagery, as well as to  
132 a GNSS reference recorded after the englacial channel had melted out a year later  
133 (table 1).

## 134 2 Materials and Methods

### 135 2.1 Drifter platforms

136 Two different drifter platforms were used in this study: A submersible drifter  
137 for path reconstruction and a GNSS surface drifter for reference measurements.

138 A detailed description of the submersible drifter can be found in (Alexander,  
139 Kruusmaa, et al., 2020). The device is a 12 cm long, 4 cm diameter and 143 g heavy,  
140 neutrally buoyant tube (see fig. 2(a)-2(d)). It contains three 2 bar pressure sensors  
141 (MS5837-2BA, TE Connectivity, Switzerland) with a sensitivity of 0.02 mbar and a  
142 9 degree of freedom (DOF) IMU (BNO055, Bosch Sensortec, Germany). The sam-  
143 pling rate for the pressure sensors and the IMU is 100 Hz. All data is stored at a 16  
144 GB microSD card in hex format.

145 The GNSS surface drifter, described in more detail in (Tuhtan et al., 2020)  
146 and (Alexander et al., n.d.), served as reference. It is a 0.35 kg heavy, positively  
147 buoyant drifter consisting of a 25 cm diameter foam floater enclosing a waterproof  
148 box (see fig. 2(e)-2(h)). Inside the box is a custom-built printed circuit board (PCB)  
149 containing a Bosch BNO055 IMU and a NEO-M8T GNSS receiver powered by two  
150 rechargeable lithium batteries (type 1865, 3.7 V, 3600 mAh). All measurements are  
151 stored to a 8GB microSD card at a sampling rate of 5 Hz. The static positioning  
152 accuracy of the GNSS is  $\pm 3$  m in the horizontal and  $\pm 10$  m in the vertical direction  
153 (Tuhtan et al., 2020).

### 154 2.2 Study site and fieldwork

155 The fieldwork was conducted on Austre Brøggerbreen, an approximately 5 km  
156 long valley glacier, located outside the research settlement Ny-Ålesund on the Nor-  
157 wegian administrated Svalbard archipelago. The glacier has several englacial chan-  
158 nels, which have been studied and described regularly over the past 20 years (Vatne,  
159 2001; Stuart et al., 2003; Vatne & Irvine-Fynn, 2016; Kamintzis et al., 2018). Our  
160 fieldwork focused on the lower englacial channel, which was mapped 20 years earlier  
161 and described in (Vatne, 2001; Stuart et al., 2003). Two different drifter platforms  
162 (GNSS surface drifters (Tuhtan et al., 2020) and submersible drifters (Alexander,  
163 Kruusmaa, et al., 2020)) were deployed from a former moulin marked with a red star  
164 on the map in figure 1(c) between 30.06.2019 and 05.07.2019 during the period of  
165 the main spring snow melt. In total we deployed the submersible drifters 24 times.  
166 All drifters were recovered by hand from the river in the glacier forefield (orange cir-  
167 cle on the map in figure 1(c)), using survival suits. Data was downloaded to a field

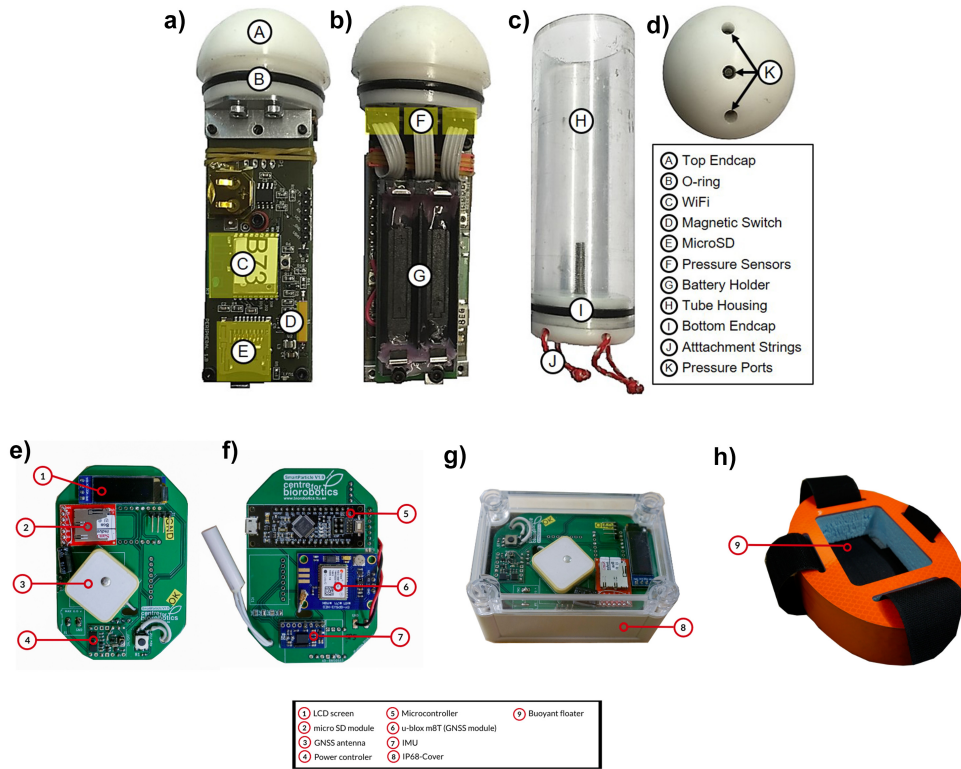


Figure 2: Two different drifter platforms have been used in this study: A submersible drifter and a GNSS surface drifter. (a)-(d) show the submersible drifter and (e)-(h) the GNSS surface drifter. (a) Side view showing the submersible drifter electronics. (b) Side view showing the reverse side of the electronics board including the battery holder and pressure sensors. (c) Polycarbonate tube housing of the submersible drifters with attachment strings for balloons used for manual buoyancy adjustment. (d) Top view facing the cap, showing the ports for each of the three pressure sensors. (e) Side view showing the GNSS surface drifter electronics with LCD screen SD storage, GNSS antenna and power controller. (f) Side view showing the reverse side of the GNSS surface drifter electronics with microcontroller, GNSS receiver and IMU. (g) The electronics of the GNSS surface drifter are sealed in a waterproof box. (h) The box gets placed at the center of a 30 cm long float.

168 computer using WiFi. We revisited the englacial channel on 19.08.2020 and deployed  
 169 a GNSS enabled surface drifter (Tuhtan et al., 2020) to gather a GNSS path of the  
 170 now melted-out channel (orange path in fig. 1(c)). We additionally deployed both  
 171 drifter platforms on a small supraglacial stream further upstream from the englacial  
 172 channel (shown in light blue in fig. 1(c)) on 02.07.2019.

### 173 2.3 Model description

174 The general workflow of our subsurface flow path reconstruction is shown in  
 175 figure 3. The input data for the noise removal and feature extraction phases are  
 176 the gyroscope, acceleration and magnetometer readings of the submersible drifter’s  
 177 inertial measurement unit (IMU). The output of the model is the average flow path  
 178 in UTM coordinates (WGS84 UTM 32 North) with pressure distribution. The IMUs  
 179 used (Alexander, Kruusmaa, et al., 2020; Tuhtan et al., 2020) provide internally cal-  
 180 culated quaternions as well as Euler angels. For flow path reconstruction additional  
 181 input is needed to specify the start and end points of the path. In our case those are  
 182 GPS referenced deployment and recovery coordinates of the drifters. The processing  
 183 and modeling of data from one deployment took on average 20 minutes. For this, we  
 184 used MATLAB 2019b on a consumer laptop (1.8 GHz Intel Core i7, 8 GB RAM).

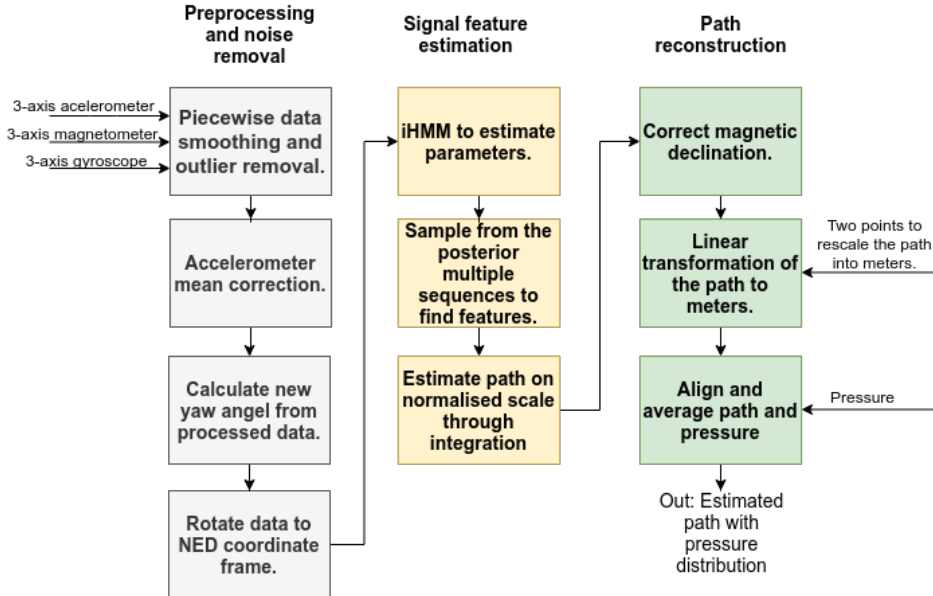


Figure 3: The proposed model workflow diagram. The model applies an infinite hidden Markov model (iHMM) on the IMU data to detect signal features.

### 185 2.4 Preprocessing and noise removal

186 The data from each submersible drifter deployment was manually clipped to  
 187 only account the time between deployment and recovery. Each deployment dataset  
 188 consisted thereby of multiple repeated measurements of 9 dof IMU sensor data (3-  
 189 axis accelerometer, 3-axis magnetometer, and 3-axis gyroscope) at 100 Hz, as well as  
 190 readings from three pressure sensors.

191 To obtain an accurate orientation estimation, the IMU data was piecewise  
 192 filtered and outliers removed. In addition, mean correction was applied to the ac-

193 celerometer data. The piecewise signal processing was thereby performed by split-  
 194 ting the data up where the mean of the signals changed significantly (Killick et al.,  
 195 2012). This allowed to subdivide the data and remove noise from each section with-  
 196 out oversmoothing the rest of the path. In each section a first order Savitzky-Golay  
 197 filter (Savitzky & Golay, 1964) was applied to both accelerometer and magnetome-  
 198 ter data. We then applied a variance based outlier filter on each section. Abrupt  
 199 changes in the acceleration behaviour lead to large errors in the rotation calculation  
 200 and hence considerable jumps in the reconstructed path. To smoothen these jumps  
 201 we applied a component-wise mean correction on the acceleration data. For this, we  
 202 calculated the mean along the whole flow path and each individual section. We then  
 203 calculated the average between the total flow path mean and each section mean and  
 204 set this average as the new mean for each section.

205 The data was rotated into earth (NED) reference frame, using the pitch and  
 206 roll angles from the device and the yaw angel calculated from the processed ac-  
 207 celerometer and magnetometer readings. The data was down sampled from 100 Hz  
 208 to 25 Hz to increase the processing speed of the model.

## 209 **2.5 Estimating the signal features using infinite hidden Markov** 210 **model**

211 Hidden Markov models (HMM) are unsupervised learning models in which the  
 212 state is not fully observable, rather it is only observed indirectly via some noisy ob-  
 213 servations. In this paper, the noisy observations are the IMU derived accelerometer,  
 214 magnetometer, and gyroscope signals. Using HMM, the aim is to find the hidden  
 215 states (features), which are assumed to be associated to the velocity. Similarly to  
 216 (Fourati et al., 2013), at the beginning of each feature, the velocity is assumed to be  
 217 zero (or close to zero).

218 First, consider a finite (regular) HMM that takes the measured IMU signals,  
 219 denoted by  $\mathbf{y} = \{y_1, y_2, \dots, y_T\}$  as input (observation sequence), and finds the hidden  
 220 state sequence  $\mathbf{s} = \{s_1, s_2, \dots, s_T\}$ , which in the scope of this paper is assumed to  
 221 be the velocity features of the water flow in the channel. In finite HMM, each state  
 222 takes a value from a finite number of states  $1, \dots, K$ , which have to be predefined. A  
 223 transition matrix  $\boldsymbol{\pi}$  describes the probabilities of moving between states. The proba-  
 224 bility of moving from state  $i$  to state  $j$  is given as  $\pi_{ij} = p(s_t = i \mid s_{t+1} = j)$  and the  
 225 initial probabilities are given by  $\pi_{0i} = p(s_1 = i)$ . In addition, there exists a param-  
 226 eter  $\phi_{s_t}$  for each state  $s_t \in \{1, \dots, K\}$ , that parametrizes the observation likelihood for  
 227 that state given by  $y_t \mid s_t \sim F(\phi_{s_t})$ . The observation likelihood describes the prob-  
 228 ability of an observation  $y_t$  being generated from a state. Hence, the HMM can be  
 229 written as  $\{\pi_0, \boldsymbol{\pi}, \boldsymbol{\phi}, K\}$ . The joint distribution over hidden states  $\mathbf{s}$  and observations  
 230  $\mathbf{y}$ , given the parameters  $\{\pi_0, \boldsymbol{\pi}, \boldsymbol{\phi}, K\}$ , can be written as:

$$p(\mathbf{s}, \mathbf{y} \mid \pi_0, \boldsymbol{\pi}, \boldsymbol{\phi}, K) = \prod_{t=1}^T p(s_t \mid s_{t+1}) p(y_t \mid s_t). \quad (1)$$

231 The finite HMMs have two big limitations: First, maximum likelihood esti-  
 232 mations do not consider the complexity of the model. This makes underfitting and  
 233 overfitting hard to avoid. Second, the model has to be specified in advance. This  
 234 means, that even though the hidden states are unknown, the number of different  
 235 states has to be predefined. Due to the complexity of the model, predefineding it is  
 236 complex, as one has to choose the number of different features in the glacial channels  
 237 based only on the measured IMU data.

238 We address these limitations by applying an infinite hidden Markov model  
 239 (iHMM) (Beal et al., 2002). The iHMM uses Dirichlet processes to define a non-

240 parametric Bayesian analysis on HMM, allowing countably infinite number of hidden  
 241 states, thus permitting automatic determination of the number of hidden states.  
 242 Therefore, not knowing how many different features are present in the glacial chan-  
 243 nel is not a problem anymore.

244 In a HMM, the transition matrix  $\boldsymbol{\pi}$  is a  $K \times K$  matrix, where  $K$  is predefined.  
 245 In iHMM, by contrast  $K \rightarrow \infty$ . To allow this and to complete the Bayesian descrip-  
 246 tion, the priors are defined using hierarchical Dirichlet processes (HDP), allowing to  
 247 have distributions over hyper-parameters and making the model more flexible.

248 The HDP are a set of DPs coupled through a shared random base measure  
 249 drawn from a DP. That is, each  $G_k \sim \text{DP}(\alpha, G_0)$  with a shared base measure  $G_0$  and  
 250 a concentration parameter  $\alpha > 0$ . The shared base measure can be thought of as the  
 251 mean of  $G_k$  and the concentration parameter  $\alpha$  controls the variability around  $G_0$ .  
 252 In addition, the shared base measure is also given a DP prior  $G_0 \sim \text{DP}(\gamma, H)$ , where  
 253  $H$  is a global base measure. The formal definition of the iHMM is given as:

$$\beta \sim \text{GEM}(\gamma) \tag{2}$$

$$\boldsymbol{\pi}_k \mid \beta \sim \text{DP}(\alpha, \beta) \tag{3}$$

$$\phi_k \sim H \tag{4}$$

$$s_t \mid s_{t-1} \sim \text{Multinomial}(\boldsymbol{\pi}_{s_{t-1}}) \tag{5}$$

$$y_t \mid s_t \sim F(\phi_{s_t}). \tag{6}$$

254 Where  $\text{DP}(\alpha, \beta)$  is a Dirichlet Process, the parameter  $\beta$  is a hyperparameter  
 255 for the DP that is distributed according to the stick-breaking construction noted as  
 256  $\text{GEM}(\cdot)$  (Sethuraman, 1994). The indicator variable  $s_t$  is sampled from the multi-  
 257 nomial distribution. Finally, priors are also put on hyperparameters  $\alpha$  and  $\gamma$ . As  
 258 there are no strong beliefs about the hyperparameters, a common practice is to use  
 259 gamma hyperpriors.

260 To find the two sets of unknowns, i.e., the hidden states and the hyperparam-  
 261 eters, Beam sampling (Van Gael et al., 2008) is used. The Beam sampling combines  
 262 slice sampling and dynamic programming, where the first limits the number of states  
 263 considered at each time step to a finite number, and the second samples the hidden  
 264 states efficiently.

## 265 **2.6 Path reconstruction**

266 As a result, a posterior probability over sequences of observations has been  
 267 found, and multiple possible velocity feature (hidden state) sequences are sampled  
 268 from the posterior distribution. This results in a set of possible sequences of flow  
 269 features along the glacial water flow path. The path estimation is performed for  
 270 multiple feature sequences. Hence, creating multiple possible paths and an estimated  
 271 region of error.

272 The integration is done in two steps. Assuming that the velocity is zero at the  
 273 beginning of each feature, the first integration is calculated over each feature sep-  
 274 arately, setting velocity to zero at the beginning. This results in a velocity profile,  
 275 that does not correspond to the real velocity values along the path, but describes  
 276 the changes in velocity along the path. The second integration is performed over the  
 277 new velocity profile and normalised, resulting in the glacier water flow path topol-  
 278 ogy map on a normalised scale. After correcting magnetic declination, the resulting  
 279 topology map can be rescaled back to earth coordinates through a linear transfor-  
 280 mation. This transformation can be found by knowing two distinct points along

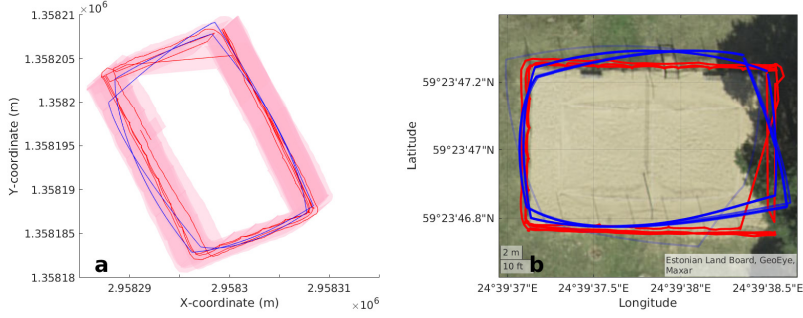


Figure 4: A rectangular volleyball field serves as ‘Proof of concept’ case. (a) Estimated rectangular path with standard deviations. Blue: The reconstruction. Red: GNSS surface drifter path. All values are given in UTM coordinates. (b) Estimation of the volleyball field with optical satellite image in the background. The reconstruction is shown in blue and the dGPS reference path in red.

Table 1: Overview of the reconstruction cases and the validation methods.

Reconstruction	Reference for validation
Rectangular path (volleyball field)	dGPS GNSS surface drifter
Supraglacial channel	GNSS surface drifter
Englacial channel	1999 GPR track 2019 Planet imagery 2020 GNSS surface drifter

281 the path, in our case, the deployment and recovery positions. The reconstructed  
 282 paths from each deployment and their pressure distributions are aligned and aver-  
 283 aged. The alignment was thereby performed using dynamic time warping (DTW)  
 284 (Sakoe & Chiba, 1978), such that each subsequent signal was aligned with the mean  
 285 of previous signals. Overall this resulted in the pressure distribution and estimated  
 286 average reconstruction of the hydrological flow path.

## 287 2.7 Validation cases

288 To validate our model we used a volleyball field in Tallinn (Estonia) as a first  
 289 ‘proof of concept’ case. For this we took two GNSS surface drifters (Tuhtan et al.,  
 290 2020) and two submersible drifters (Alexander, Kruusmaa, et al., 2020) and walked  
 291 one round at the outer edge of the field. Additionally we recorded the same track  
 292 using a Trimble R4 dGPS device.

293 As second validation case, we used a supraglacial channel on Austre  
 294 Brøggerbreen (see figure 1(c)), where we deployed both drifter platforms (sub-  
 295 mersible drifters and GNSS surface drifters) on the 2nd of July 2019 by hand and  
 296 recovered them further downstream.

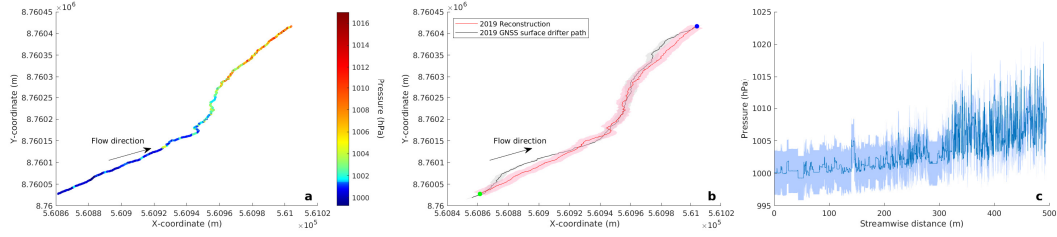


Figure 5: Supraglacial path reconstruction. (a) Reconstructed supraglacial track in UTM coordinates with pressure distribution in hPa. (b) Estimation of the supraglacial track (red) with standard deviations (pink) in UTM coordinates. The GNSS reference is shown in black and the average error of the GNSS recordings in light gray. The deployment and recovery points are denoted with green and blue circles respectively. The arrow denotes the flow direction. (c) Average water pressure with standard deviation along the estimated stream-wise distance of the supraglacial channel.

### 297 3 Results

#### 298 3.1 Known rectangular path

We initially validated our method by the reconstruction of a rectangular path (volleyball field, size 14x23 m) with a known GNSS reference (see figure 4). The path had a total dGPS (Trimbel R4) derived length of 74.0 m. Our reconstruction, based on two IMU datasets, resulted in an average path length of 70.1 m, an under-estimation of the real length by -5.3%. We further calculated the position error for each point as

$$Error = \sqrt{(p_x(t) - \hat{p}_x(t))^2 + (p_y(t) - \hat{p}_y(t))^2} \quad (7)$$

299 where  $p_x(t)$  and  $p_y(t)$  are the coordinates measured via dGPS and  $\hat{p}_x$  and  $\hat{p}_y$  are  
 300 the estimated points from the reconstruction. The resulting average absolute error,  
 301 based on the 10 nearest points is 0.14 m and the maximum error 2.9 m. This equals  
 302 an average error of 1% for the width and 0.6% for the length of the rectangle, with  
 303 maximum errors of 20.7% for the width and 12.6% for the length.

#### 304 3.2 Supraglacial calibration

305 We then tested our approach with the reconstruction of a supraglacial channel  
 306 with known geometry (fig. 1(c)). As a reference, we used an averaged path (see ta-  
 307 ble 1), derived from GNSS surface drifter measurements (Tuhtan et al., 2020). The  
 308 reconstruction was based on 11 submersible drifter (Alexander, Kruusmaa, et al.,  
 309 2020) deployments. Our model reproduces a flow path, which is within 3.90 m of the  
 310 GNSS reference path (figure 5). The lowest error is thereby 2.0 m and the largest  
 311 deviation from the reference path is 11.10 m, based on the average of 10 nearest  
 312 points. As fig. 6 shows, the average error from our reconstruction converges after 6  
 313 datasets (one drifter deployment needed per dataset). The total length of the GNSS  
 314 reference track is 449 m, whereas the reconstructed path is 478 m long, equal to an  
 315 overestimation by 6.5%. The resulting flow path allows further to spatially reference  
 316 the pressure measurements of the drifters. The obtained pressure distribution map  
 317 shows pressure variations along the channel with zones of higher pressures occur-  
 318 ring mainly in the lower part of the channel and in areas where the channel changes  
 319 direction.

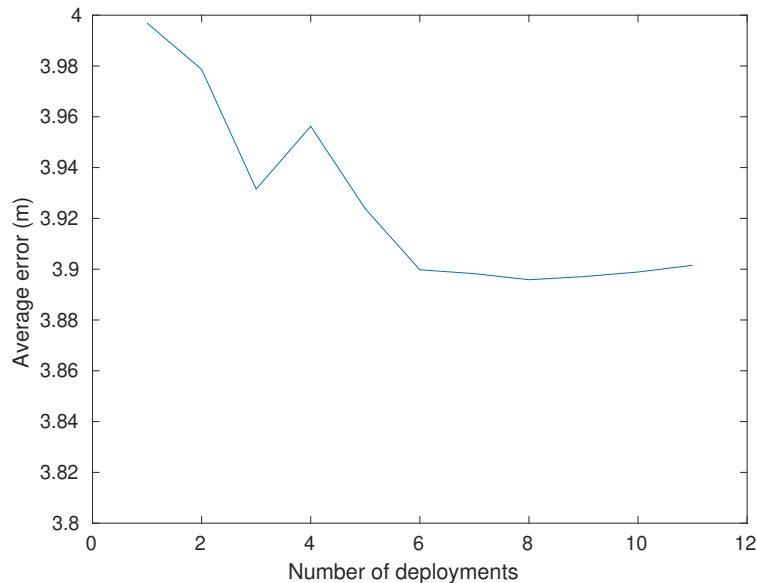


Figure 6: Convergence of the average error for the supraglacial channel reconstruction with respect to the number of deployments.

320

### 3.3 Englacial channel reconstruction

321

322

323

324

325

326

327

328

329

330

The submersible drifter deployments for the reconstruction were collected in July 2019. A revisit of the field site in August 2020 allowed to map the flow path of the channel with the GNSS surface drifter, as the roof of the channel had mostly melted away and transformed the former englacial channel into a deeply incised supraglacial channel, which was only partly ice covered. The reconstruction from the IMU data, collected in 2019 (6 deployments), leads to the mean flow path shown in figure 7(b). The figure also shows the comparison between a GNSS reference track measured a year later in summer 2020 and a GPR measurement from 1999. The shape of the reconstructed flow path thereby resembles the shape of both, the 2020 GNSS reference and the 1999 GPR track from (Stuart et al., 2003).

331

332

333

334

335

336

337

338

339

340

341

342

343

The overall average position error (based on equation 7) of the reconstructed englacial channel and the proglacial river, compared to the 2020 GNSS reference path for the channel, as well as the 2019 satellite derived proglacial river path (see figure 7), is 12.1 m. The englacial channel part of the reconstruction has an average error of 13.3 m compared to the 2020 GNSS reference (see tab. 1 for an overview of used references). From the englacial outlet through the canyon (fig. 1(f)) and the proglacial river up to the recovery point (fig. 1(g)), the average error of the reconstructed path is 10.9 m compared to the satellite reference path. The path length of the 2020 GNSS reference track (1 deployment) from the englacial channel is 544.8 m. The section after the outlet of the channel through the canyon and the proglacial river measures 290 m on the satellite imagery. Our model returns a total path length of 1027 m from deployment point to recovery point. The channel section is thereby 651 m long and the part through the canyon and the proglacial river 376 m.

344

345

346

The mean pressure recorded by the drifters is 1011.7 mbar with a standard deviation of 3.4 mbar (0.3%). The spatial pressure distribution map (fig. 7(a)) reveals one zone of higher pressure shortly before the englacial channel exits into the open

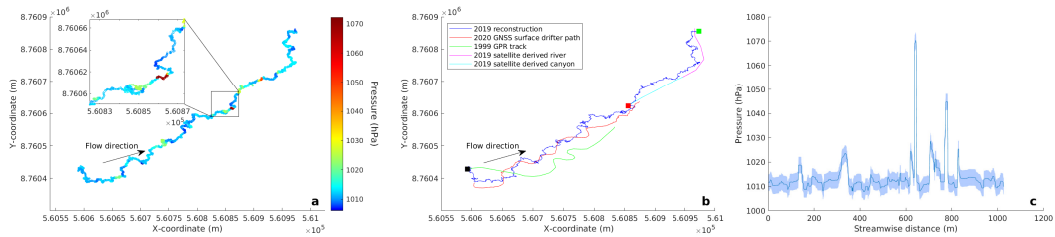


Figure 7: Englacial channel reconstruction. (a) Estimated average track of the englacial channel in UTM coordinates with pressure distribution in hPa. (b) Estimated englacial track in UTM coordinates based on the 2019 IMU data in blue alongside GNSS drifter reference measured in 2020 in red. Further shown are the mapped canyon and proglacial river from optical Planet imagery (acquisition date 09.07.20219, (Team Planet, 2017)), as well as the 1999 GPR map traced from (Stuart et al., 2003). The Black square denotes the deployment point and the green square the recovery location. Additionally shown is the location of the start of the canyon at the end of the englacial channel (red square). (c) Average water pressure with standard deviation along the estimated stream-wise distance of the englacial channel.

347 canyon. The average water pressure thereby reaches up to 1.07 bar, compared to  
 348 maximum values of 1.3 bar recorded by the submersible drifters.

#### 349 4 Discussion and Conclusions

350 We showed the topological reconstruction of a supra-, as well as an englacial  
 351 channel on Austre Brøggerbreen (Svalbard) and used these reconstructions to spa-  
 352 tially reference the pressure distributions within these channels.

353 The results of the supraglacial channel show a progressively enhanced sequenc-  
 354 ing of meander bends in the lower part of the channel. Aligning the pressures to  
 355 the reconstructed flow path reveals zones of larger pressure variations in the same  
 356 section of the channel. This is in accordance with our previous work (Alexander,  
 357 Kruusmaa, et al., 2020), where we showed the connection between larger pressure  
 358 variations and morphological features in the channel, such as step-pool sequences  
 359 and meander bends. Visual observations during the fieldwork of this study further  
 360 confirm this connection, as several meander bends, as well as step-pool sequences,  
 361 existed in the lower part. This is also in good agreement with the results of the  
 362 topological reconstruction of the channel.

363 It is important to emphasize, that the GNSS reference used in the supraglacial  
 364 channel reconstruction is not the most accurate. The static positioning error of  
 365 the used GNSS receivers is  $\pm 3$  m (Tuhtan et al., 2020), with the dynamic position-  
 366 ing error, in a highly turbulent supraglacial stream, certainly being higher. The  
 367 used GNSS reference path is additionally an aligned average of 26 single tracks  
 368 (Alexander et al., n.d.), thereby over-smoothing several meander-bends and therefore  
 369 smoothing the real channel geometry. An average error of 3.90 m for the reconstruc-  
 370 tion versus the GNSS reference path is therefore likely below the accuracy of the  
 371 GNSS reference track itself. The over-smoothing of the GNSS reference path also  
 372 explains, why the reconstructed path's length is 6.5% longer compared to the GNSS  
 373 reference. We therefore estimate the error of our reconstruction to be closer to the  
 374 values calculated for the rectangular validation case, where a dGPS reference path  
 375 was available.

376 The flow path of the englacial channel, investigated in this study, has been  
377 repeatedly mapped by previous studies. (Stuart et al., 2003) utilized GPR to draw  
378 a map of the channel (shown in fig. 1(c)), whereas (Vatne, 2001) used speleological  
379 investigations, providing a very simple map in his publication. These studies allow  
380 us to approximately assess the feasibility of our reconstructed flow path, as well as  
381 the evolution of the channel as both previous investigations took place twenty years  
382 earlier.

383 We have further revisited the englacial channel in late summer 2020. Heavy  
384 summer melt, in both 2019 and 2020, has led to the melt-out of the englacial chan-  
385 nel, which by the end of 2020 was not longer an englacial channel, but rather a  
386 deeply incised canyon. This has allowed us to collect a GNSS reference path using  
387 a GNSS enabled drifter (Tuhtan et al., 2020; Alexander et al., n.d.) and further vi-  
388 sually inspect parts of the channel. Both the 2020 GNSS reference path, the 1999  
389 GPR reconstruction and our 2019 reconstruction are shown in figure 7(b).

390 The qualitative comparison between the 1999 GPR reconstruction of the  
391 englacial channel from (Stuart et al., 2003) and our GNSS surface drifter mea-  
392 surements from 2020 show good accordance in the overall shape of the flow path. It  
393 is visible that the channel developed by both vertical and lateral incision, thereby  
394 keeping its' overall shape over the 21 years spanning between the two investigations.  
395 Our 2019 reconstruction is well within this overall shape, reflecting the same qual-  
396 itative flow path. The error of our reconstruction is 12.1 m, which is higher than  
397 the error of the supraglacial reconstruction. We assume that this is mainly due to  
398 the lack of an accurate reference path. The positional accuracy of the obtained 2020  
399 GNSS path is likely much lower than in the supraglacial case, as the quality of the  
400 received GNSS signal in the up to 20 m deep, narrow and partly ice covered canyon  
401 was not the best. The used satellite reference for the canyon (fig. 1(f)) and the  
402 proglacial river (fig. 1(g)) was mapped on planet imagery, which have a positional  
403 accuracy of less than 10 m RMSE (Team Planet, 2017). The canyon was thereby  
404 barely visible on the imagery leading to a straight reference track instead of a me-  
405 andering one, as the real geometry would have implied (see fig. 1(f)). We therefore  
406 attribute the higher calculated error of the englacial channel to the lower accuracy of  
407 the used reference paths compared to the validation cases.

408 The length of the flow path of the englacial reconstruction is 1027 m, much  
409 longer than the sum of the GNSS and the satellite reference path of 834.8 m. The  
410 GNSS reference path is, however, missing the first section of the englacial channel  
411 after deployment due to changed water pathways between 2019 and 2020. Based on  
412 handhold GPS measurements, this length difference is estimated to be 85 m. This  
413 leaves a difference of 107.2 m between reference track length and the reconstruc-  
414 tion or an overestimation of the track by 11.4%. This does, however, not take into  
415 account that the satellite reference path is underestimating the real track length.  
416 Therefore the real length error of our reconstruction is likely much lower. On the  
417 other hand, the drifter based reconstruction could also overestimate the channel  
418 length. Our reconstruction is based on the distance travelled by the drifters. As they  
419 can get stuck in eddies or travel from one side of the channel to the other, the recon-  
420 structed path becomes longer than the real channel. This can also be seen in very  
421 wobbly sections of the channel reconstruction in figure 7(a).

422 The pressures recorded by the submersible drifters in the englacial channel  
423 show flow under atmospheric conditions. Pressurized flow conditions, where the wa-  
424 ter flows uphill as encountered by (Stuart et al., 2003), do not longer exist within  
425 the channel. The average error of the pressure data is, with 3.4 mbar, similar to  
426 our previous work (Alexander, Kruusmaa, et al., 2020), thus very low. Within  
427 the englacial channel itself, one zone of abrupt and high pressure change exists  
428 shortly before the channel exits into the canyon. Similar to pressure peaks studied in

(Alexander, Kruusmaa, et al., 2020), we interpret this as the presence of a step-pool sequence with a large step riser. This interpretation was confirmed by speleological investigations in 2018, where a roughly 2.5 m high step riser was found at the same location.

In this study we used a relatively low number of deployments (11 for the supraglacial channel and 6 for the englacial channel) for the reconstruction with an average error of 3.90 m and 12.1 m, respectively. The average error calculations for the supraglacial channel (figure 6) show that the error converges at 6 deployments. The decrease of the average error with increasing deployment number is, however, so low (2.5%) that a single deployment would already lead to sufficient precision. Using the values for the mean pressure and its standard deviation, leads to a precision of 0.66% with just one deployment, according to equation 4 in (Alexander, Kruusmaa, et al., 2020). This shows, that our approach is able to produce a highly precise topological reconstruction and spatial pressure distribution from just one deployment. As we have lost one submersible drifter out of 24 deployments at the englacial channel (95.8% recovery rate) and encountered technical problems (e.g. drifter switched off during deployment, damaged pressure recordings) with quite some of the retrieved datasets (utility rate of only 25%), we estimate that at least 5 submersible drifter deployments will be needed in the field in order to obtain the topology of an englacial channel.

At the current stage we are only able to produce the planar topology of the flow path. A full 3D reconstruction was not possible because the used IMUs (Alexander, Kruusmaa, et al., 2020) do not correct for the gravity vector. Removing the gravity vector in the post-processing stage introduces additional uncertainty and therefore renders an inaccurate elevation track. We are, however, optimistic that we will be able to do full 3D reconstructions in an improved version of our method, by collecting additional vertical reference data and accounting for the error introduced by the gravity vector. The current model is also not able to calculate the numerical velocity, as the model operates largely on a normalised space. Another development step will therefore be to also reconstruct flow velocities utilizing the time stamp of the IMU recordings alongside the reconstructed path length. Mapping flow velocities alongside pressure distribution would provide an additional input for numerical flow models.

Overall, we have developed a method that is able to produce decent flow path reconstructions with only two given coordinates. As our method can already be run with the data from just one submersible drifter deployment and on a consumer laptop, it will be practical for a variety of field applications. This suggests that our results might have larger implications, not only for glaciology, but also for subsurface flow studies in general.

#### 4.1 Data archival

All data will be made publicly available at the end of the peer-review process.

#### Acknowledgments

The fieldwork for this project was funded by the H2020 INTERACT Transnational Access project DeepSense 2019, University of Oslo Industrial Liason, University of Oslo Garpen Stipend, the Department of Geosciences University of Oslo, the Research Council of Norway funded MAMMAMIA project (grant number 301837 MAMMAMIA: Multi-scale multi-method analysis of mechanisms causing ice acceleration) and the Svalbard Environmental protection fund (17/31). This research was further funded by the European Research Council (grant no. ICEMASS) and the Research Council of Norway (grant no. 223254 – NTNU AMOS). Fieldwork in

479 2020 was funded by the Research Council of Norway via an Arctic Field Grant to  
 480 AA (Dynamics of glacial channels, RiS ID 11423). This study is a contribution to  
 481 the Svalbard Integrated Arctic Earth Observing System (SIOS). We further on  
 482 acknowledge support from the team of the NPI Sverdrup station, particularly Vera  
 483 Sklet, during the fieldwork. Asko Ristolainen and Astrid Tesaker helped during the  
 484 2020 field campaign. The drifters used in this study were originally designed by Jef-  
 485 frey A. Tuhtan and Juan Francisco Fuentes-Perez. We also acknowledge Jeffreys’  
 486 contribution during the 2019 fieldwork for this study and his valuable input for  
 487 model development and scientific discussions. The GNSS surface drifter figure was  
 488 provided by Kerstin Alexander.

## 489 References

- 490 Alexander, A., Kruusmaa, M., Tuhtan, J. A., Hodson, A., Schuler, T., & Kääh, A.  
 491 (2020). Pressure and inertia sensing drifters for glacial hydrology flow path  
 492 measurements. *The Cryosphere*, *14*, 1009–1023.
- 493 Alexander, A., Obu, J., Schuler, T. V., Kääh, A., & Christiansen, H. H. (2020).  
 494 Subglacial permafrost dynamics and erosion inside subglacial channels driven  
 495 by surface events in svalbard. *The Cryosphere*, *14*(11), 4217–4231. Re-  
 496 trieved from <https://tc.copernicus.org/articles/14/4217/2020/> doi:  
 497 10.5194/tc-14-4217-2020
- 498 Alexander, A., Tuhtan, J., Kruusmaa, M., Schuler, T., & Kääh, A. (n.d.). Spa-  
 499 tiotemporal distribution of water flow velocities, accelerations and ice melt  
 500 rates inside a small supraglacial channel derived from drifter measurements. *In*  
 501 *preparation*.
- 502 Andrews, L. C., Catania, G. A., Hoffman, M. J., Gulley, J. D., Lüthi, M. P., Ryser,  
 503 C., ... Neumann, T. A. (2014). Direct observations of evolving subglacial  
 504 drainage beneath the greenland ice sheet. *Nature*, *514*(7520), 80–83.
- 505 Bælum, K., & Benn, D. I. (2011). Thermal structure and drainage system of a small  
 506 valley glacier (tellbreen, svalbard), investigated by ground penetrating radar.  
 507 *The Cryosphere*, *5*(1), 139.
- 508 Bagshaw, E. A., Burrow, S., Wadham, J. L., Bowden, J., Lishman, B., Salter, M.,  
 509 ... Nienow, P. (2012). E-tracers: Development of a low cost wireless technique  
 510 for exploring sub-surface hydrological systems. *Hydrological Processes*, *26*(20),  
 511 3157–3160.
- 512 Bagshaw, E. A., Lishman, B., Wadham, J. L., Bowden, J. A., Burrow, S. G., Clare,  
 513 L. R., & Chandler, D. (2014). Novel wireless sensors for in situ measurement  
 514 of sub-ice hydrologic systems. *Annals of glaciology*, *55*(65), 41–50.
- 515 Beal, M. J., Ghahramani, Z., & Rasmussen, C. E. (2002). The infinite hidden  
 516 markov model. In *Advances in neural information processing systems* (pp.  
 517 577–584).
- 518 Björnsson, H. (1975). Subglacial water reservoirs, jökulhlaups and volcanic eruptions.  
 519 *Jökull*, *25*, 1–14.
- 520 Engelhardt, H., Humphrey, N., Kamb, B., & Fahnestock, M. (1990). Physical condi-  
 521 tions at the base of a fast moving antarctic ice stream. *Science*, *248*(4951), 57–  
 522 59.
- 523 Flowers, G. E. (2015a). Modelling water flow under glaciers and ice sheets. *Proceed-*  
 524 *ings of the Royal Society A: Mathematical, Physical and Engineering Sciences*,  
 525 *471*(2176), 20140907.
- 526 Flowers, G. E. (2015b). Modelling water flow under glaciers and ice sheets. *Proceed-*  
 527 *ings of the Royal Society A: Mathematical, Physical and Engineering Sciences*,  
 528 *471*(2176), 20140907.
- 529 Fountain, A. G., & Walder, J. S. (1998). Water flow through temperate glaciers. *Re-*  
 530 *views of Geophysics*, *36*(3), 299–328.
- 531 Fourati, H., Manamanni, N., Afllal, L., & Handrich, Y. (2013). Position estimation

- 532 approach by complementary filter-aided imu for indoor environment. In *2013*  
 533 *European control conference (ecc)* (pp. 4208–4213).
- 534 Gimbert, F., Tsai, V. C., Amundson, J. M., Bartholomaeus, T. C., & Walter, J. I.  
 535 (2016). Subseasonal changes observed in subglacial channel pressure, size, and  
 536 sediment transport. *Geophysical Research Letters*, *43*(8), 3786–3794.
- 537 Gulley, J. D., Benn, D. I., Screatton, E., & Martin, J. (2009). Mechanisms of  
 538 englacial conduit formation and their implications for subglacial recharge.  
 539 *Quaternary Science Reviews*, *28*(19-20), 1984–1999.
- 540 Hansen, L. U., Piotrowski, J. A., Benn, D. I., & Sevestre, H. (2020). A cross-  
 541 validated three-dimensional model of an englacial and subglacial drainage  
 542 system in a high-arctic glacier. *Journal of Glaciology*, *66*(256), 278–290.
- 543 Holmlund, P. (1988). Internal geometry and evolution of moulins, storglaciären, swe-  
 544 den. *Journal of Glaciology*, *34*(117), 242–248.
- 545 Hooke, R. L. (1989). Englacial and subglacial hydrology: a qualitative review. *Arctic*  
 546 *and Alpine Research*, *21*(3), 221–233.
- 547 Hubbard, B., & Nienow, P. (1997). Alpine subglacial hydrology. *Quaternary Science*  
 548 *Reviews*, *16*(9), 939–955.
- 549 Hubbard, B., Sharp, M. J., Willis, I. C., Nielsen, M., & Smart, C. C. (1995). Bore-  
 550 hole water-level variations and the structure of the subglacial hydrological  
 551 system of haut glacier d’arolla, valais, switzerland. *Journal of Glaciology*,  
 552 *41*(139), 572–583.
- 553 Iken, A. (1972). Measurements of water pressure in moulins as part of a movement  
 554 study of the white glacier, axel heiberg island, northwest territories, canada.  
 555 *Journal of Glaciology*, *11*(61), 53–58.
- 556 Iken, A., & Bindschadler, R. A. (1986). Combined measurements of subglacial wa-  
 557 ter pressure and surface velocity of findelengletscher, switzerland: conclusions  
 558 about drainage system and sliding mechanism. *Journal of Glaciology*, *32*(110),  
 559 101–119.
- 560 Kamintzis, J. E., Jones, J. P. P., Irvine-Fynn, T. D. L., Holt, T. O., Bunting, P.,  
 561 Jennings, S. J. A., ... Hubbard, B. (2018). Assessing the applicability of ter-  
 562 restrial laser scanning for mapping englacial conduits. *Journal of Glaciology*,  
 563 *64*(243), 37–48.
- 564 Killick, R., Fearnhead, P., & Eckley, I. A. (2012). Optimal detection of changepoints  
 565 with a linear computational cost. *Journal of the American Statistical Associa-*  
 566 *tion*, *107*(500), 1590–1598.
- 567 Montello, D. R. (2005). *Navigation*. Cambridge University Press.
- 568 Nanni, U., Gimbert, F., Vincent, C., Gräff, D., Walter, F., Piard, L., & Moreau, L.  
 569 (2020). Quantification of seasonal and diurnal dynamics of subglacial chan-  
 570 nels using seismic observations on an alpine glacier. *The Cryosphere*, *14*(5),  
 571 1475–1496.
- 572 Pörtner, H.-O., Roberts, D. C., Masson-Delmotte, V., Zhai, P., Tignor, M.,  
 573 Poloczanska, E., ... others (2019). Ipcc special report on the ocean and  
 574 cryosphere in a changing climate. *IPCC Intergovernmental Panel on Climate*  
 575 *Change (IPCC)*.
- 576 Röthlisberger, H. (1972). Water pressure in intra-and subglacial channels. *Journal of*  
 577 *Glaciology*, *11*(62), 177–203.
- 578 Sakoe, H., & Chiba, S. (1978). Dynamic programming algorithm optimization for  
 579 spoken word recognition. *IEEE transactions on acoustics, speech, and signal*  
 580 *processing*, *26*(1), 43–49.
- 581 Savitzky, A., & Golay, M. J. E. (1964). Smoothing and differentiation of data by  
 582 simplified least squares procedures. *Analytical chemistry*, *36*(8), 1627–1639.
- 583 Schaap, T., Roach, M. J., Peters, L. E., Cook, S., Kulesa, B., & Schoof, C. (2020).  
 584 Englacial drainage structures in an east antarctic outlet glacier. *Journal of*  
 585 *Glaciology*, *66*(255), 166–174.

- 586 Sethuraman, J. (1994). A constructive definition of dirichlet priors. *Statistica sinica*,  
587 639–650.
- 588 Shreve, R. L. (1972). Movement of water in glaciers. *Journal of Glaciology*, 11(62),  
589 205–214.
- 590 Stone, D. B., & Clarke, G. K. C. (1996). In situ measurements of basal water  
591 quality and pressure as an indicator of the character of subglacial drainage  
592 systems. *Hydrological Processes*, 10(4), 615–628.
- 593 Stuart, G., Murray, T., Gamble, N., Hayes, K., & Hodson, A. (2003). Character-  
594 ization of englacial channels by ground-penetrating radar: An example from  
595 austre brøggerbreen, svalbard. *Journal of Geophysical Research: Solid Earth*,  
596 108(B11).
- 597 Team Planet. (2017). *Planet application program interface: In space for life on*  
598 *earth*. Retrieved from <https://api.planet.com>
- 599 Thrun, S. (1998). Learning metric-topological maps for indoor mobile robot naviga-  
600 tion. *Artificial Intelligence*, 99(1), 21–71.
- 601 Thrun, S., Burgard, W., & Fox, D. (1998). A probabilistic approach to concurrent  
602 mapping and localization for mobile robots. *Autonomous Robots*, 5(3-4), 253–  
603 271.
- 604 Tuhtan, J., Alexander, A., Kruusmaa, M., & Fuentes-Pérez, J. (2020). Multiscale  
605 change detection in a supraglacial stream using surface drifters. In *Proceedings*  
606 *of the international conference on river flow 2020*. Delft.
- 607 Van Gael, J., Saatci, Y., Teh, Y. W., & Ghahramani, Z. (2008). Beam sampling for  
608 the infinite hidden markov model. In *Proceedings of the 25th international con-*  
609 *ference on machine learning* (pp. 1088–1095).
- 610 Vatne, G. (2001). Geometry of englacial water conduits, austre brøggerbreen, sval-  
611 bard. *Norsk Geografisk Tidsskrift*, 55(2), 85–93.
- 612 Vatne, G., & Irvine-Fynn, T. (2016). Morphological dynamics of an englacial chan-  
613 nel. *Hydrology and Earth System Sciences*, 20(7), 2947–2964.
- 614 Vieli, A., Jania, J., Blatter, H., & Funk, M. (2004). Short-term velocity varia-  
615 tions on hansbreen, a tidewater glacier in spitsbergen. *Journal of Glaciology*,  
616 50(170), 389–398.